

Dry Transfer of van der Waals Crystals to Noble Metal Surfaces To Enable Characterization of Buried Interfaces

Andrey Krayev,[†] Connor S. Bailey,[‡] Kiyoung Jo,[§] Shuo Wang,^{||} Akshay Singh,[⊥] Thomas Darlington,[#] Gang-Yu Liu,^{||} Silvija Gradecak,[⊥] P. James Schuck,[#] Eric Pop,[‡] and Deep Jariwala^{*,§,||}

[†]Horiba Scientific, Novato, California 94949, United States

[‡]Department of Electrical Engineering, Stanford University, Stanford, California 94305, United States

[§]Department of Electrical and Systems Engineering, University of Pennsylvania, Philadelphia, Pennsylvania 19104, United States

^{||}Department of Chemistry, University of California, Davis, California 95616, United States

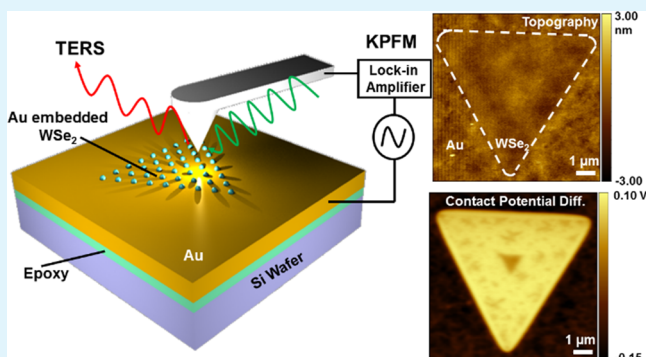
[⊥]Department of Materials Science and Engineering, Massachusetts Institute of Technology, Cambridge, Massachusetts 02139, United States

[#]Department of Mechanical Engineering, Columbia University, New York, New York 10027, United States

Supporting Information

ABSTRACT: Two-dimensional (2D) transition-metal dichalcogenides (TMDCs) have been explored for many optoelectronic applications. Most of these applications require them to be on insulating substrates. However, for many fundamental property characterizations, such as mapping surface potential or conductance, insulating substrates are nonideal as they lead to charging and doping effects or impose the inhomogeneity of their charge environment on the atomically thin 2D layers. Here, we report a simple method of residue-free dry transfer of 2D TMDC crystal layers. This method is enabled via noble-metal (gold, silver) thin films and allows comprehensive nanoscale characterization of transferred TMDC crystals with multiple scanning probe microscopy techniques. In particular, intimate contact with underlying metal allows efficient tip-enhanced Raman scattering characterization, providing high spatial resolution (<20 nm) for Raman spectroscopy. Further, scanning Kelvin probe force microscopy allows high-resolution mapping of surface potential on transferred crystals, revealing their spatially varying structural and electronic properties. The layer-dependent contact potential difference is clearly observed and explained by charge transfer from contacts with Au and Ag. The demonstrated sample preparation technique can be generalized to probe many different 2D material surfaces and has broad implications in understanding of the metal contacts and buried interfaces in 2D material-based devices.

KEYWORDS: van der Waals materials, transition-metal dichalcogenides, near field, buried interfaces, Raman spectroscopy, TERS



INTRODUCTION

The advent of layered two-dimensional (2D) crystals with van der Waals interlayer interactions has opened up new research avenues in materials and surface science as well as condensed matter physics and device engineering.^{1–5} While 2D materials such as graphene and transition-metal dichalcogenides (TMDCs) have been extensively studied both for fundamental science and device applications, a majority of these studies have occurred on insulating substrates, which are critical for field-effect devices.^{6,7} However, most practical 2D devices tend to also have metal interfaces (e.g., contacts), which are subjects of much debate, and numerous studies have been dedicated to understand this interface.^{2,8–16} To date, little is known about this buried interface using direct microscopic and spectroscopic measurements. Even less is known in the context of 2D materials where the band structure changes as a function of

thickness and the interfaces are highly sensitive to contamination. Metal contacts to semiconductors are ubiquitous in all solid-state devices and more recently have been critical for the case of TMDCs for ultrathin photovoltaics.^{17–23} Thorough understanding of physical phenomena occurring at metal/2D semiconductor interfaces is therefore not only a matter of pure academic interest but is also an equally important problem for prospective applications.

Direct exfoliation using an adhesive tape method from bulk crystals and polymer-assisted transfer of chemical vapor deposition (CVD)-grown crystals are two of the most popular techniques for TMDC sample preparation and transfer.

Received: June 5, 2019

Accepted: September 12, 2019

Published: September 12, 2019

However, both suffer from the same unavoidable problem, that is, the introduction of polymer contamination. This can significantly alter the distribution of the surface potential and even topography, when puddles of low-molecular-weight polymer spread across the sample surface with time, compromising the quality of the contacts and heterojunctions.²⁴ An alternative, cleaner method has been introduced recently,²⁵ wherein a thin gold film is evaporated onto bulk TMDC crystals, using it to preferentially exfoliate monolayers and few layers and then etched away in KI/I₂ solution, thus avoiding polymer contamination. Similarly evaporated Ni thin films have been used to exfoliate wafer scale monolayers from multilayer films.²⁶ Despite obvious advantages of such a method, the etching solution and some atomic metal residues are unavoidable. Another interesting technique has been published recently on freshly evaporated, smooth gold film-assisted exfoliation of large, hundreds of microns across, mono- to few-layer TMDC crystals.²⁷ Scotch tape-assisted exfoliation from bulk TMDC crystals was a crucial step in this reported methodology. While the reported approach enables intimate contact between the freshly cleaved surface of the TMDC crystal and the gold substrate across large areas, it would be inapplicable for the transfer of the CVD-grown single to few layer TMDC crystals since it becomes increasingly difficult to attain an intimate mechanical contact (1–2 Å) across large areas between two rigid surfaces such as Si wafers. Further, the peeling/exfoliation in this case is critically dependent on surface contamination of the Au film and interlayer interactions between the van der Waals materials and the top layer in contact with Au.

In this work, we propose a facile method, also based on the use of noble metals such as silver or gold, which is suitable for transfer of CVD-grown TMDCs, regardless of layer thickness or preparation type. The transferred TMDC samples on noble metals have pristine interfaces on both sides, that is, the contact with noble metal as well as the exposed interface. This allows the characterization of transferred TMDCs and their buried interface with few nanometer-scale resolution using scanning probe microscopy (SPM) techniques. Further, being in close proximity with a noble metal such as Au or Ag, we can use plasmonic probe tips to perform near-field spectroscopy characterization via tip-enhanced Raman spectroscopy (TERS). Our results demonstrate that the noble metal-based one-step transfer process produces atomically clean buried interfaces and suggests that the charge transfer between noble metals and TMDCs can vary significantly depending on the metal and number of layers of the TMDC.

EXPERIMENTAL SECTION

TMDC crystals, both WSe₂²⁸ and MoS₂²⁹ were grown via the standard powder precursor-based CVD techniques. Gold deposition via thermal evaporation was performed in a Model DV502-A high vacuum evaporator (Denton Vacuum Inc., Moorestown, NJ); e-beam-assisted gold deposition was done in a Model PVD-75 e-beam evaporator (Kurt Lesker). All scanning probe characterizations including atomic force microscopy (AFM), Kelvin probe force microscopy (KPFM), far-field Raman spectroscopy, and tip-enhanced Raman spectroscopy (TERS) characterizations were performed in either XploRA-Nano or LabRam-Nano AFM-Raman systems (Horiba Scientific). All other details are discussed in the Supporting Information.

RESULTS AND DISCUSSION

To perform this study, we investigated a set of TMDC samples (here WSe₂²⁸ and MoS₂²⁹) grown by CVD. Details of the synthetic procedures can be found in the corresponding section of the Supporting Information. All data shown in the figures below is based on WSe₂; hence, all references to TMDC in the figures are for WSe₂ but can be generalized to MoS₂ and possibly other TMDCs as well. The data on MoS₂ is presented in the Supporting Information. The step-by-step procedure of the proposed noble metal-assisted transfer method is shown in Figure 1a,b (full process and cross section

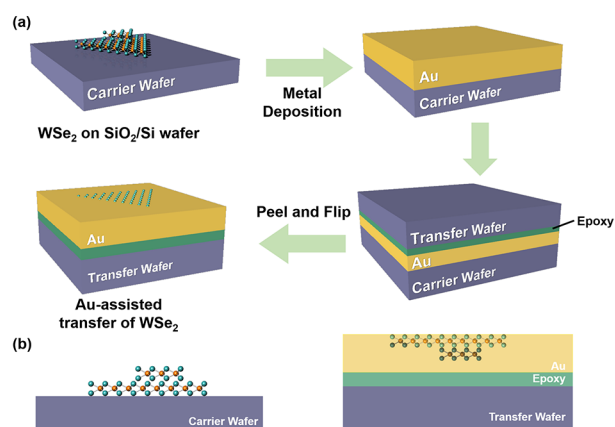


Figure 1. (a) Step-by-step scheme of gold (silver)-assisted transfer of CVD-grown TMDC crystals from the original SiO₂/Si carrier wafer onto a transfer wafer by use of thermal epoxy as the bonding layer. (b) Cross-sectional view of the samples before and after transfer.

of initial and final stages of the samples, respectively). First, a thin gold (100 nm) or silver film (55 nm Ag covered by 50 nm Au) is directly thermally deposited on top of the CVD-grown TMDC crystals on the SiO₂/Si substrate (carrier wafer) without any pretreatment. Our preference for thermal evaporation is because it is known to be less detrimental and less likely to introduce defects as compared to e-beam evaporation.^{30,31} Following evaporation, a piece of silicon wafer (transfer wafer) is glued to the noble metal film using a thin layer of thermal epoxy (Epo-Tek 375, Epoxy Technology). After the epoxy layer cures and achieves its final hardness, the top silicon piece is peeled upward, which results in stripping of the gold/silver film together with the TMDC crystals from the substrate. This epoxy-based peeling procedure has been discussed in detail in prior publications.^{23,32} It is worth noting that, in this multilayer stack, the adhesion at the epoxy–gold and TMDC–gold interfaces is stronger than that at the SiO₂–gold, TMDC–SiO₂, and TMDC–TMDC interfaces (for the case of bilayer and thicker flakes). Hence, this peeling and transfer process works as intended.

The resulting samples after peeling were characterized using multimode SPM comprising scanning Kelvin Probe Force microscopy (KPFM) analysis cross-correlated with tip-enhanced Raman scattering (TERS) mapping (Figure 2a).^{12,16,33} As a result of this one-step transfer and peeling process, we obtained samples with topography seen in Figure 2b where TMDC crystals embedded into the gold layer were exposed on the side originally facing the SiO₂ substrate. The RMS roughness on the TMDC is 0.44 nm, whereas that on the

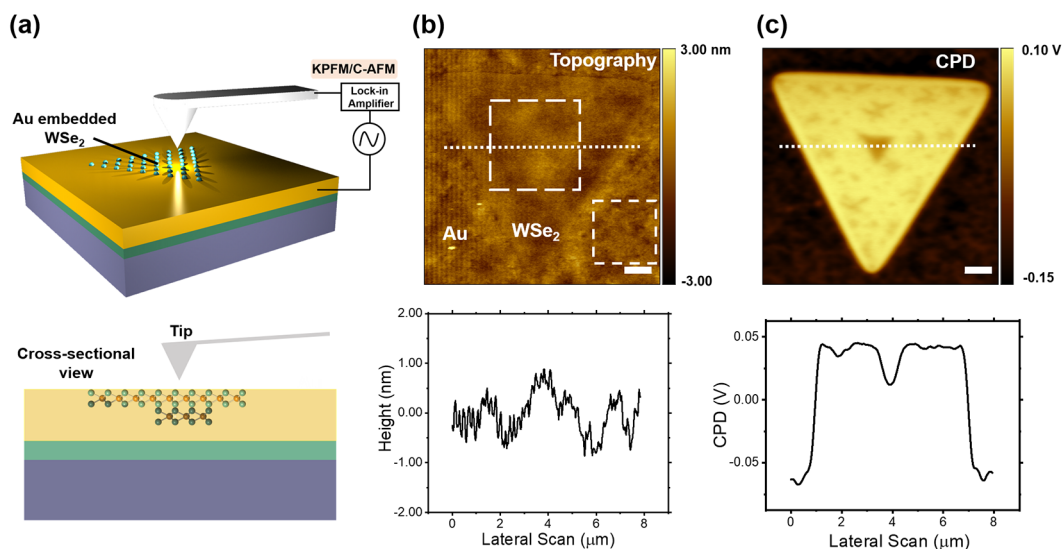


Figure 2. (a) Isometric view of the schematic of the measurement setup (top) and cross-sectional view (bottom). (b) Topography image of a WSe₂ triangular crystal transferred with Au showing flat topography (RMS roughness ~ 0.44 on both Au and WSe₂ on Au) with a faint triangular outline. The bottom shows a line-cut profile corresponding to the white line in the top image, showing little variation in topography across the TMDC and Au interface. (c) Concurrently acquired CPD image of the same TMDC triangle showing a sharp contrast between the Au substrate and the WSe₂ region. Additional contrast of bilayer islands or contaminants buried underneath the monolayer is also visible. The bottom panel shows a line-cut profile shown by the same dashed white line, which shows reduced surface potential for the central triangular bilayer island, as well as other irregular dendritic features interspersed across the surface. The inset scale bar in panels (b) and (c) is 1 μm .

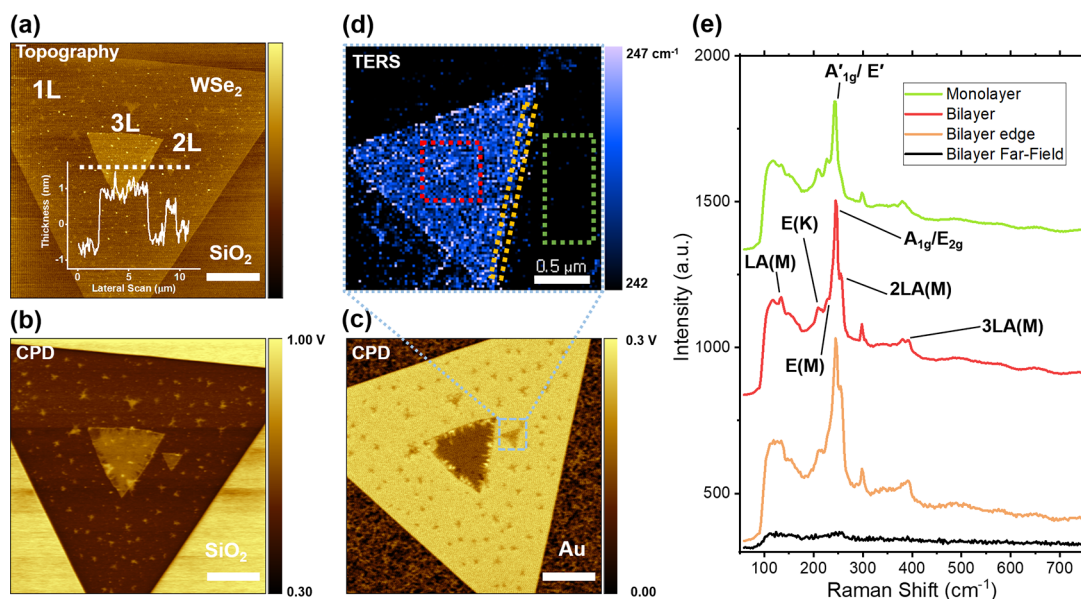


Figure 3. (a) Topography of an as-grown crystal on SiO₂ and (b) corresponding CPD data. The topography analysis clearly shows mono-, bi-, and trilayer heights of the various islands on SiO₂, while the CPD map shows higher positive potential for SiO₂ than monolayer WSe₂. The higher or more positive potentials of the bilayer and trilayer vs the monolayer are also clearly visible. (c) CPD map of the same portion of the sample after Au-assisted transfer showing a flip in the sign of the relative surface potential difference between flake and substrate as well as between the mono- and multilayer areas. (d) TERS map of the blue-dashed square in panel (a) showing a higher TERS signal from the bilayer island than from the monolayer. The map shows the average peak position of the complex peak in the 200–265 cm^{-1} range (the map indicates the average of peak position of the complex peak at each point), which efficiently reflects the intensity of the 2LA(M) peak relative to the main A_{1g}/E_{2g} band. (e) Averaged TERS spectra from the monolayer part (green), inner area of the bilayer (red), and the edges of the bilayer island (orange). The black spectrum is the far-field Raman signal collected when the tip was oscillating about 25–30 nm away from the surface, with the same integration time as the TERS spectra, clearly evidencing strong TERS enhancement and the lack of any noticeable enhancement effect purely from the gold substrate. Inset scale bars in panels (a), (b), and (c) are 5 μm and 500 nm in panel (d).

Au is 0.43 nm. This indicates that both surfaces are equally smooth and adapt to the smoothness of the wafer on which they are deposited. We observed a number of interesting

heterogeneities that varied depending on specific TMDCs. In the following, we discuss in-depth results obtained on WSe₂ transferred with gold and silver and will compare them to the

results obtained on gold-transferred MoS₂ presented in the Supporting Information.

For the case of CVD-grown WSe₂ samples, after transfer, we observed shallow topography and a number of features in contact potential difference (CPD) maps (Figure 2c). Primarily, in the center of the triangular crystals, we frequently observed perfectly concentric triangular areas with lower surface potential (about 70–100 mV lower) as seen in Figure 2c. Such concentric triangular features most probably correspond to a thicker region of second or higher number of layers nucleating from the center of the first layer, which often appears in large CVD-grown TMDC crystals.²⁸ Note that, because the few-layer-thick inner triangle faces “down” into the noble metal layer, the topography is flat but changes are still measurable using CPD. In addition to the central island with a decreased value of CPD, we observed irregularly shaped fractal features that also showed a lower value of the surface potential compared to the adjacent area, though the value of the CPD drop was somewhat smaller (around 15–20 mV) than that of the central island (70–100 mV). Such fractal or dendrite-shaped features that may appear at certain growth conditions have been experimentally observed and theoretically explained earlier.³⁴ Our results in Figure 2 suggest that, even though topography shows no noticeable features, the atomically thin nature of the semiconductor allows “peering through” the top layer via electrostatic potential interactions to image the potential of the buried bi(multi)layers on the first grown WSe₂ layer.

A unique feature of these transferred samples^{28,29} is that TMDC crystals are naturally in very close proximity to plasmonic metal surfaces. Therefore, the use of a plasmonic TERS probe provides us with a capability to acquire topography, surface potential, and Raman spectroscopy information from the same sample area with the same probe at <20 nm spatial resolution. The TERS map collected around the central triangular and fractal features showed a significantly different Raman response from locations with decreased values of the surface potential (Figure S1), therefore confirming that the chosen characterization techniques can adequately address nanoscale heterogeneities in transferred samples.

Based on our successful transfer and nanoscale characterization of the first batch of samples, we perform follow-up experiments aiming to track the changes occurring as a result of transfer on the same WSe₂ crystal. We performed comparative measurements on a representative CVD-grown WSe₂ crystal that featured a trilayer core in the center and several small bilayer islands of both fractal and perfectly triangular shape. Topography and CPD images of the as-grown crystal are shown in Figure 3a,b, respectively. The core triangle and bilayer islands of the as-grown crystal on the SiO₂–Si substrate showed a higher surface potential than the monolayer part. The monolayer nature of the majority of the crystal was confirmed both by topography and the presence of a strong photoluminescence (PL) peak at ~770 nm (~1.61 eV) acquired before transfer (Figure S2 in the Supporting Information).

After gold-assisted transfer, the CPD image looked very similar to the one shown in Figure 2, where the overall CPD of the WSe₂ crystal was more positive in value than that of the adjacent gold, while bi- and trilayer islands showed lower surface potentials (210 mV for bilayer, 140 mV for trilayer) than the adjacent monolayer (270 mV) (Figure 3c). The origin of this behavior of the CPD signal will be elaborated further in

the discussion section. The TERS map collected over one of such buried bilayer regions of the triangular crystal in Figure 3d showed increased intensities of longitudinal acoustic modes LA(M), 2LA(M), and 3LA(M) in the Raman spectra compared to the adjacent monolayer (Figure 3e), which is not surprising, taking into account that these LA modes are closely associated with defects as has been reported in the literature.³⁵ It is important to note that all observed peaks in the TERS spectra of gold-transferred WSe₂ showed a significant red shift ~8 cm⁻¹ as compared to literature precedent.³⁶ Even though a systematic study of the origins of the observed red shift is beyond the scope of this manuscript, we can speculate that this shift of Raman bands in gold-transferred WSe₂ crystals may be caused by intrinsic bonding or interface strain-related phenomena, for example, the Au–Se physical bonding interaction or the inevitable mechanical stress in WSe₂ that may appear in the process of gold deposition and subsequently during TMDC removal from SiO₂. We rule out large charge transfer-induced hole doping as discussed below, which typically results in small blue shifts.³⁷ We also rule out SERS or similar effects since we measure both near-field and far-field Raman signals for comparison. The far-field signal (black spectrum in Figure 3e) is acquired with the tip significantly (about 25–30 nm) away from the sample, which does not show any noticeable Raman enhancement effect. Additional far-field spectra on Au and Ag are shown in the Supporting Information (Figure S8).

We also note that the overall intensity of TERS spectra decreases as the mapping progresses, as compared to mechanically exfoliated samples (see the Supporting Information, Figure S7). This may be an indication of the presence of some growth-related contaminants at the SiO₂–WSe₂ interface, which remains on the exposed surface of the transferred crystal and aggregates at the apex of the TERS probe, corroding the chemically less stable Ag, causing a decrease in its efficiency.^{38,39} We further note that our CPD and TERS observations in Figure 3 were reproducible across other samples. TERS signals of the bi- and trilayer islands were qualitatively similar with minor differences. As was noted above, bilayer islands featured an increased intensity of peaks associated with LA(M) phonons and a slight blue shift of E(M) and E(K) modes. Similar observations were made in the central trilayer island, with an even stronger increase of the intensity of the 2LA(M) peak (Figure S1). It is interesting to note that we did not observe any PL in crystals transferred to gold, even though the Raman bands were strongly enhanced in our TERS spectra. We attribute this to the immediate proximity and therefore strong electronic coupling of WSe₂ to the metal substrate, which provides a channel for nonradiative decay of excitons.

Based on the above results, it was important to understand whether this transfer process is limited to gold only or it can be extended to other noble metals such as silver. Silver (Ag) is a desirable metal for a number of reasons: first, it has a significantly lower work function compared to gold⁴⁰ and therefore provides certain flexibility in terms of engineering desired electronic properties of the metal–TMD interface. Second, by alloying silver and gold, one can gradually change the work function of the substrate from 5.1 eV in the case of pure polycrystalline gold to 4.3 eV for pure polycrystalline silver.^{40,41}

Similar to the case of Au-assisted transfer, we thermally deposited 55 nm of Ag followed by 50 nm of Au (to prevent

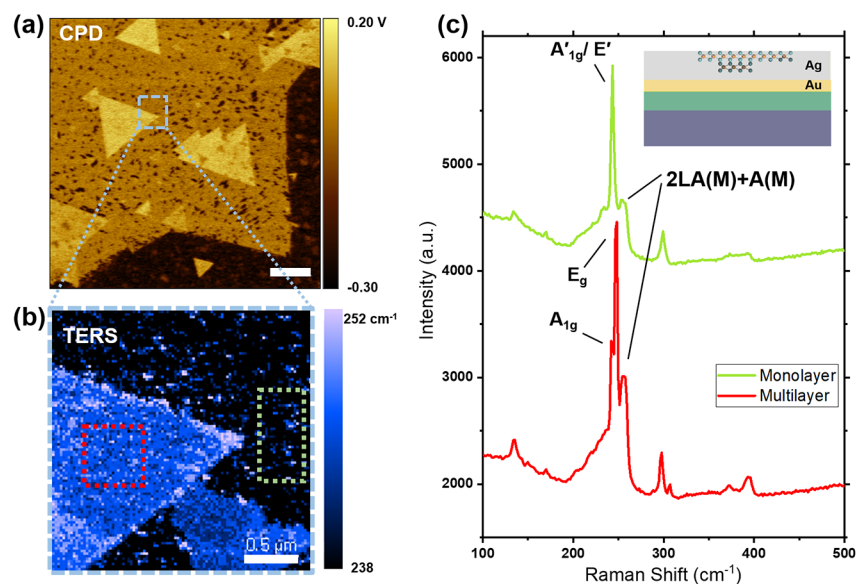


Figure 4. (a) CPD image of a WSe₂ crystal transferred with silver immediately after stripping (scale bar = 5 μm) (b) TERS map corresponding to the peak position of a complex peak within the 200–260 cm⁻¹ range in spectra shown in panel (c). The map indicates the average of the peak positions of the complex peak at each point. (c) Averaged TERS spectra from multilayer (red) and monolayer (green) parts of the crystal.

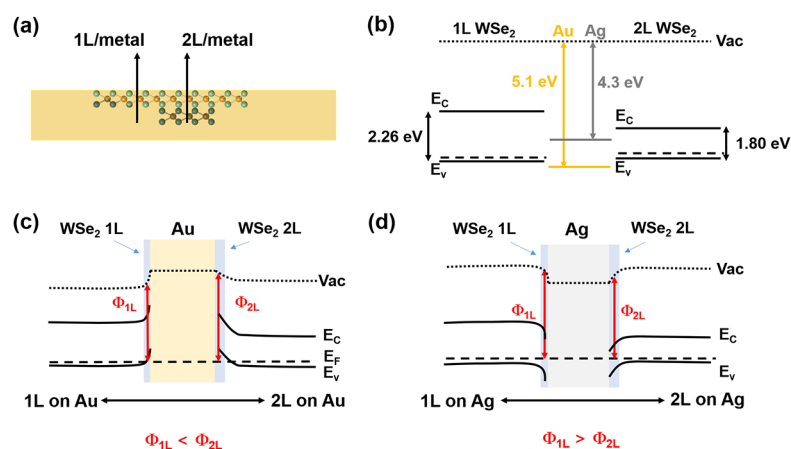


Figure 5. (a) Schematic cross section of the WSe₂ embedded in a Au layer with arrows showing directions along which band diagrams have been drawn. (b) Band alignments of monolayer (1L) and bilayer (2L) WSe₂ with that of Au and Ag. Projected equilibrium band diagrams on Au (c) showing Ohmic band alignment and on Ag (d) showing Schottky band alignment.

silver degradation in ambient conditions) onto the CVD-grown WSe₂ and stripped the crystals following the procedure described above. The transferred regions are shown in Figure 4. The CPD profile (Figure 4a) and TERS characterization (Figure 4b) of the Ag-transferred WSe₂ crystals revealed a number of unexpected differences compared to the crystals that were transferred using Au. First, immediately after the transfer, the value of the CPD of WSe₂ monolayer crystals was higher relative to the Ag substrate, taking into account that the Fermi level of Ag should be higher than that of WSe₂. Second, the CPD of the monolayer part of crystals transferred with Ag was observed to have greater spatial nonuniformity in the CPD as compared to the case of transfer using Au. This could likely be the result of the polycrystalline nature of the silver film and the significant difference of the work function of silver for different crystalline facets. Alternatively, silver being much more chemically active compared to gold might react with local contaminants on the surface of WSe₂ crystals, which

would cause an inevitable change in the local CPD value. Another interesting feature was the fact that the CPD of the multilayer islands (~100 mV) proved to be more positive (greater than) compared to adjacent monolayers (30 mV), unlike the case of the crystals transferred with Au. The details of work function change and doping are elaborated in the discussion below.

The TERS response (633 nm pump laser) of Ag-transferred WSe₂ was also somewhat different from the case of Au: first, we observed a fairly intense peak at 299 cm⁻¹, which softens to 297 cm⁻¹ for multilayer islands and corresponds to the 295 cm⁻¹ peak reported previously¹⁶ in WSe₂ crystals exfoliated on silver. The second interesting feature was a strong split of the E_g and A_{1g} modes in multilayer islands, with an A_{1g} peak position shifting to 248 from 243 cm⁻¹ of the partially overlapping E'/A_{1'} peak in the case of monolayer, which has also been reported earlier.³⁶

To further investigate the nature of the interface and generalize this transfer technique, we applied it to CVD-grown crystals of MoS₂ on SiO₂/Si²⁹ (Figures S4–S6) in the Supporting Information, wherein the Au was sputter-deposited and thermally evaporated, thereby elucidating subtle differences in the buried interface in different metal evaporation schemes. Our experiments suggest that thermally evaporated samples lead to clear observation of resonant Raman as opposed to sputtered samples suggesting higher crystalline quality of the buried TMDC interface. A detailed comparison will be the subject of a separate study. In addition, Au-assisted transfer was applied not only to CVD-grown TMDCs but also to directly exfoliated TMDCs (Figure S7 in the Supporting Information). In particular, exfoliated WSe₂ by the adhesive tape method was successfully flipped through the Au-assisted transfer. The CPD value reaches the maximum at the monolayer and gradually decreases as the layer becomes thicker, which corresponds well to the result of transferred CVD-grown WSe₂ discussed above.

Overall, our proposed transfer approach is proven to be very general and applicable across a broad spectrum of metal deposition techniques and TMDC types. Subtle differences and variation between TMDCs and metal deposition techniques can be explained by the level of contamination, surface oxidation, and bonding between the chalcogen and the noble metal, as detailed in the Supporting Information.

Buried electronic interfaces in 2D materials and metal–semiconductor contacts have been the subject of much debate with numerous research papers and review articles being published. However, issues such as the extent of charge transfer between the two, chemical stability of the contact, and band bending are still far from clear. Our study shows that these quantities can be directly measured and imaged using a scanning probe if the interface is clean and flat, which is enabled by our transfer technique (Figure 5a). From the interpretation of our CPD data, we note that the CPD contrast in as-grown and transferred samples cannot be explained solely by variations of the Fermi level in mono- and multilayered parts of the TMDC crystals and the number of layers, and correspondingly, the thickness of the crystal should also play an important role. Purely electrostatic considerations suggest that the close proximity of metals to semiconductors also leads to charge transfer and formation of depletion regions.^{15,42}

Taking all these into account, we can interpret our CPD data on three different substrates, namely, SiO₂, Au, and Ag, as follows. For the case of the as-grown WSe₂ on the SiO₂ substrate, the oxide is known to have a fixed positive charge.^{43,44} This fixed positive charge is screened by the WSe₂ monolayer as it grows on it. Therefore, the CPD signal drops to a smaller positive value. Then, as the bilayer (of same orientation) grows on the monolayer, the band gap substantially changes (reduces). As per the literature precedent of band gap evolution in WSe₂ as a function of layer thickness,^{45,46} the conduction band goes down significantly and the valence band is almost unaffected,⁴⁷ which forms a type II alignment (Figure 5b).^{46,48,49} However, the doping level in the flake^{50,51} must remain the same so that the Fermi level moves down. As a consequence, the work function for the bilayer goes up and the CPD value rises to be more positive. The same effect occurs for the trilayer except that the jump is smaller, as the rate of gap reduction reduces with increasing thickness.^{45,46}

When one deposits Au on the TMDC, the Au forms a very intimate contact, both physically and electronically with the TMDC. Au has a large work function (5.1 eV for polycrystalline gold⁴⁰) and therefore forms an Ohmic contact with p-doped WSe₂.^{48,52} Thus, the WSe₂ in close proximity to Au will be under hole accumulation (positive charge), and hence, the CPD rises compared to the Au substrate and reaches 270 mV (Figure 5c). As the WSe₂ thickness increases, the band gap diminishes and the Fermi level goes further down. However, the electronic contact remains Ohmic in nature, and WSe₂ stays under accumulation (positive charge) except that now the positive charge starts getting screened by the increasing number of layers, causing less band bending and corresponding higher work function. Thus, there is a drop in CPD, which is defined as

$$V_{\text{CPD}} = \frac{\Phi_{\text{tip}} - \Phi_{\text{sample}}}{q} \quad (1)$$

where Φ is the respective work function and q is the elementary charge.

The case of Ag is conceptually similar to Au, except that Ag has a much lower work function than Au, forming a Schottky contact instead of Ohmic and thus causing hole depletion in the WSe₂. This leads to lower CPD of WSe₂ (30 mV) than that of Au-transferred WSe₂ (270 mV) (Figure 5d). Further, with increasing thickness, a decrease in the Fermi level occurs. This is due to the band gap change (reduction),⁴⁷ which results in reduction of the work function to cause a further increase of the CPD value in a bilayer and thicker regions, compared to that of a monolayer.

Based on the above results and discussion, we believe that our noble metal-assisted transfer technique for TMDCs helps deepen our understanding of the metal–TMDC buried interface. In particular, it informs us that the interface contact potential is highly sensitive and depends not only on the number of layers of TMDC but also on the deposition conditions (see the Supporting Information, Figures S4–S6). Further, even though the TMDC layers can act as impenetrable atomically thin barriers, their contact or junction with underlying media leaves a surface potential fingerprint, which can be detected by KPFM and TERS, opening the door to subsurface characterization of novel heterostructures and devices.

CONCLUSIONS

In summary, we demonstrate a robust, simple, and contamination-free transfer technique of CVD-grown TMDC crystals to metallic (gold or silver) substrates. The sample surfaces produced by this technique show smooth topography (RMS roughness = 0.44 nm) making them ideal for plasmonic/conductive tip-based SPM and TERS characterization. Cross-correlated CPD and TERS characterization of CVD-grown WSe₂ crystals showed that islands of bi- and trilayers buried under the monolayer showed significantly different values of the surface potential compared to the adjacent monolayer, suggesting strong electronic coupling to the underlying metal, while TERS spectra of these thicker islands featured an increased intensity of LA phonon modes at the M point, which in turn is an indication of the increased defect concentration.

Our transfer method seems to be particularly useful for investigation of air- and moisture-sensitive 2D materials like

tellurides, perovskites, niobium and tantalum chalcogenides, or even black phosphorus. Gold/silver deposited on top of exfoliated or CVD-grown crystals can serve as a protection barrier, thereby allowing sample exposure to characterization for barely minutes, if not seconds. This presents a unique advantage that can open up new avenues for sample analysis and characterization for atomically thin materials.

■ ASSOCIATED CONTENT

Supporting Information

The Supporting Information is available free of charge on the ACS Publications website at DOI: 10.1021/acsami.9b09798.

Synthesis method of CVD-grown WSe₂ and MoS₂; metal deposition, topography, and PL spectrum of as-grown WSe₂ crystal; CPD and TERS mapping of WSe₂ after Au- and Ag-assisted transfer; CVD-grown MoS₂ after Au-assisted transfer; direct exfoliated WSe₂ after Au-assisted transfer (PDF)

■ AUTHOR INFORMATION

Corresponding Author

*E-mail: dmj@seas.upenn.edu

ORCID

Silvija Gradecak: 0000-0003-4148-4526

Eric Pop: 0000-0003-0436-8534

Deep Jariwala: 0000-0002-3570-8768

Notes

The authors declare no competing financial interest.

■ ACKNOWLEDGMENTS

This work was carried out in part at the Singh Center for Nanotechnology at the University of Pennsylvania and at the Stanford Nanofabrication Facility, which are supported by the National Science Foundation (NSF) National Nanotechnology Coordinated Infrastructure Program grant NNCI-1542153. D.J. and K.J. acknowledge primary support for this work by the U.S. Army Research Office under contract number W911NF1910109. D.J. also acknowledges support from Penn Engineering Start-up funds, National Science Foundation (DMR-1905853) and University of Pennsylvania Materials Research Science and Engineering Center (MRSEC) (DMR-1720530). C.S.B. acknowledges support from the NSF Graduate Fellowship. C.S.B. and E.P. were also supported in part by the Air Force Office of Scientific Research grant FA9550-14-1-0251, by the NSF EFRI 2-DARE grant 1542883, and by the Stanford SystemX Alliance. Authors are grateful for efforts of Jinshui Miao and Huiqin Zhang for metal deposition during sample preparation.

■ REFERENCES

- (1) Das, S.; Robinson, J. A.; Dubey, M.; Terrones, H.; Terrones, M. Beyond Graphene: Progress in Novel Two-Dimensional Materials and Van Der Waals Solids. *Annu. Rev. Mater. Res.* **2015**, *45*, 1–27.
- (2) Fiori, G.; Bonaccorso, F.; Iannaccone, G.; Palacios, T.; Neumaier, D.; Seabaugh, A.; Banerjee, S. K.; Colombo, L. Electronics Based on Two-Dimensional Materials. *Nat. Nanotechnol.* **2014**, *9*, 768–779.
- (3) Novoselov, K. S.; Fal'ko, V. I.; Colombo, L.; Gellert, P. R.; Schwab, M. G.; Kim, K. A Roadmap for Graphene. *Nature* **2012**, *490*, 192–200.

- (4) Stanford, M. G.; Rack, P. D.; Jariwala, D. Emerging Nanofabrication and Quantum Confinement Techniques for 2D Materials Beyond Graphene. *Npj 2D Mater. App.* **2018**, *2*, 20.
- (5) Brar, V. W.; Sherrott, M. C.; Jariwala, D. Emerging Photonic Architectures in Two-Dimensional Opto-Electronics. *Chem. Soc. Rev.* **2018**, *47*, 6824–6844.
- (6) Jariwala, D.; Marks, T. J.; Hersam, M. C. Mixed-Dimensional Van Der Waals Heterostructures. *Nat. Mater.* **2017**, *16*, 170–181.
- (7) Jariwala, D.; Sangwan, V. K.; Lauhon, L. J.; Marks, T. J.; Hersam, M. C. Emerging Device Applications for Semiconducting Two-Dimensional Transition Metal Dichalcogenides. *ACS Nano* **2014**, *8*, 1102–1120.
- (8) Smyth, C. M.; Addou, R.; McDonnell, S.; Hinkle, C. L.; Wallace, R. M. Contact Metal–MoS₂ Interfacial Reactions and Potential Implications on MoS₂-Based Device Performance. *J. Phys. Chem. C* **2016**, *120*, 14719–14729.
- (9) Domask, A. C.; Gurunathan, R. L.; Mohny, S. E. Transition Metal–MoS₂ Reactions: Review and Thermodynamic Predictions. *J. Electron. Mater.* **2015**, *44*, 4065–4079.
- (10) Liu, Y.; Guo, J.; Zhu, E.; Liao, L.; Lee, S.-J.; Ding, M.; Shakir, I.; Gambin, V.; Huang, Y.; Duan, X. Approaching the Schottky–Mott Limit in Van Der Waals Metal–Semiconductor Junctions. *Nature* **2018**, *557*, 696–700.
- (11) English, C. D.; Shine, G.; Dorgan, V. E.; Saraswat, K. C.; Pop, E. Improved Contacts To MoS₂ Transistors by Ultra-High Vacuum Metal Deposition. *Nano Lett.* **2016**, *16*, 3824–3830.
- (12) Smithe, K. K. H.; Krayev, A. V.; Bailey, C. S.; Lee, H. R.; Yalon, E.; Aslan, Ö. B.; Muñoz Rojo, M.; Krylyuk, S.; Taheri, P.; Davydov, A. V.; Heinz, T. F.; Pop, E. Nanoscale Heterogeneities in Monolayer MoSe₂ Revealed by Correlated Scanning Probe Microscopy and Tip-Enhanced Raman Spectroscopy. *ACS Appl. Nano Mater.* **2018**, *1*, 572–579.
- (13) Kappera, R.; Voiry, D.; Yalcin, S. E.; Branch, B.; Gupta, G.; Mohite, A. D.; Chhowalla, M. Phase-Engineered Low-Resistance Contacts for Ultrathin MoS₂ Transistors. *Nat. Mater.* **2014**, *13*, 1128–1134.
- (14) Kang, J.; Liu, W.; Sarkar, D.; Jena, D.; Banerjee, K. Computational Study of Metal Contacts to Monolayer Transition-Metal Dichalcogenide Semiconductors. *Phys. Rev. X* **2014**, *4*, No. 031005.
- (15) Allain, A.; Kang, J.; Banerjee, K.; Kis, A. Electrical Contacts to Two-Dimensional Semiconductors. *Nat. Mater.* **2015**, *14*, 1195–1205.
- (16) Jariwala, D.; Krayev, A.; Wong, J.; Robinson, A. E.; Sherrott, M. C.; Wang, S.; Liu, G.-Y.; Terrones, M.; Atwater, H. A. Nanoscale Doping Heterogeneity in Few-Layer WSe₂ Exfoliated onto Noble Metals Revealed by Correlated SPM and TERS Imaging. *2D Mater.* **2018**, *5*, 035003.
- (17) Furchi, M. M.; Pospischil, A.; Libisch, F.; Burgdörfer, J.; Mueller, T. Photovoltaic Effect in an Electrically Tunable Van der Waals Heterojunction. *Nano Lett.* **2014**, *14*, 4785–4791.
- (18) Koppens, F. H. L.; Mueller, T.; Avouris, P.; Ferrari, A. C.; Vitiello, M. S.; Polini, M. Photodetectors Based on Graphene, Other Two-Dimensional Materials and Hybrid Systems. *Nat. Nanotechnol.* **2014**, *9*, 780–793.
- (19) Baugher, B. W. H.; Churchill, H. O. H.; Yang, Y.; Jarillo-Herrero, P. Optoelectronic Devices Based on Electrically Tunable P–N Diodes in a Monolayer Dichalcogenide. *Nat. Nanotechnol.* **2014**, *9*, 262–267.
- (20) Memaran, S.; Pradhan, N. R.; Lu, Z.; Rhodes, D.; Ludwig, J.; Zhou, Q.; Ogunsolu, O.; Ajayan, P. M.; Smirnov, D.; Fernández-Domínguez, A. I.; García-Vidal, F. J.; Balicas, L. Pronounced Photovoltaic Response from Multilayered Transition-Metal Dichalcogenides PN-Junctions. *Nano Lett.* **2015**, *15*, 7532–7538.
- (21) Wong, J.; Jariwala, D.; Tagliabue, G.; Tat, K.; Davoyan, A. R.; Sherrott, M. C.; Atwater, H. A. High Photovoltaic Quantum Efficiency in Ultrathin Van der Waals Heterostructures. *ACS Nano* **2017**, *11*, 7230–7240.

- (22) Jariwala, D.; Davoyan, A. R.; Wong, J.; Atwater, H. A. Van Der Waals Materials for Atomically-Thin Photovoltaics: Promise and Outlook. *ACS Photonics* **2017**, *4*, 2962–2970.
- (23) Jariwala, D.; Davoyan, A. R.; Tagliabue, G.; Sherrott, M. C.; Wong, J.; Atwater, H. A. Near-Unity Absorption in Van der Waals Semiconductors for Ultrathin Optoelectronics. *Nano Lett.* **2016**, *16*, 5482–5487.
- (24) Haigh, S. J.; Gholinia, A.; Jalil, R.; Romani, S.; Britnell, L.; Elias, D. C.; Novoselov, K. S.; Ponomarenko, L. A.; Geim, A. K.; Gorbachev, R. Cross-Sectional Imaging of Individual Layers and Buried Interfaces of Graphene-Based Heterostructures and Superlattices. *Nat. Mater.* **2012**, *11*, 764.
- (25) Desai, S. B.; Madhupathy, S. R.; Amani, M.; Kiriya, D.; Hettick, M.; Tosun, M.; Zhou, Y.; Dubey, M.; Ager, J. W., III; Chrzan, D.; Javey, A. Gold-Mediated Exfoliation of Ultralarge Optoelectronically-Perfect Monolayers. *Adv. Mater.* **2016**, *28*, 4053–4058.
- (26) Shim, J.; Bae, S.-H.; Kong, W.; Lee, D.; Qiao, K.; Nezich, D.; Park, Y. J.; Zhao, R.; Sundaram, S.; Li, X.; Yeon, H.; Choi, C.; Kum, H.; Yue, R.; Zhou, G.; Ou, Y.; Lee, K.; Moodera, J.; Zhao, X.; Ahn, J.-H.; Hinkle, C.; Ougazzaden, A.; Kim, J. Controlled Crack Propagation for Atomic Precision Handling of Wafer-Scale Two-Dimensional Materials. *Science* **2018**, *362*, 665–670.
- (27) Velický, M.; Donnelly, G. E.; Hendren, W. R.; Mcfarland, S.; Scullion, D.; Debenedetti, W. J. I.; Correa, G. C.; Han, Y.; Wain, A. J.; Hines, M. A.; Muller, D. A.; Novoselov, K. S.; Abruña, H. D.; Bowman, R. M.; Santos, E. J. G.; Huang, F. Mechanism of Gold-Assisted Exfoliation of Centimeter-Sized Transition-Metal Dichalcogenide Monolayers. *ACS Nano* **2018**, *12*, 10463–10472.
- (28) Chen, J.; Bailey, C. S.; Hong, Y.; Wang, L.; Cai, Z.; Shen, L.; Hou, B.; Wang, Y.; Shi, H.; Sambur, J.; Ren, W.; Pop, E.; Cronin, S. B. Plasmon-Resonant Enhancement of Photocatalysis on Monolayer WSe₂. *ACS Photonics* **2019**, *6*, 787–792.
- (29) Smithe, K. K. H.; English, C. D.; Suryavanshi, S. V.; Pop, E. Intrinsic Electrical Transport and Performance Projections of Synthetic Monolayer MoS₂ Devices. *2D Materials* **2017**, *4*, 011009.
- (30) Blakers, A. W.; Green, M. A.; Szpitalak, T. Surface Damage Caused by Electron-Beam Metallization of High Open-Circuit Voltage Solar Cells. *IEEE Electron Device Lett.* **1984**, *5*, 246–247.
- (31) Haick, H.; Ambrico, M.; Ghabboun, J.; Ligonzo, T.; Cahen, D. Contacting Organic Molecules by Metal Evaporation. *Phys. Chem. Chem. Phys.* **2004**, *6*, 4538–4541.
- (32) Mcmorrow, J. J.; Walker, A. R.; Sangwan, V. K.; Jariwala, D.; Hoffman, E.; Everaerts, K.; Facchetti, A.; Hersam, M. C.; Marks, T. J. Solution-Processed Self-Assembled Nanodielectrics on Template-Stripped Metal Substrates. *ACS Appl. Mater. Interfaces* **2015**, *7*, 26360–26366.
- (33) Kumar, N.; Mignuzzi, S.; Su, W.; Roy, D. Tip-Enhanced Raman Spectroscopy: Principles and Applications. *EPJ Tech. Instrum.* **2015**, *2*, 9.
- (34) Nie, Y.; Liang, C.; Zhang, K.; Zhao, R.; Eichfeld, S. M.; Cha, P.-R.; Colombo, L.; Robinson, J. A.; Wallace, R. M.; Cho, K. First Principles Kinetic Monte Carlo Study on The Growth Patterns of WSe₂ Monolayer. *2D Mater.* **2016**, *3*, 025029.
- (35) Mignuzzi, S.; Pollard, A. J.; Bonini, N.; Brennan, B.; Gilmore, I. S.; Pimenta, M. A.; Richards, D.; Roy, D. Effect of Disorder on Raman Scattering of Single-Layer MoS₂. *Phys. Rev. B* **2015**, *91*, 195411.
- (36) Terrones, H.; Corro, E. D.; Feng, S.; Poumirol, J. M.; Rhodes, D.; Smirnov, D.; Pradhan, N. R.; Lin, Z.; Nguyen, M. A. T.; Elías, A. L.; Mallouk, T. E.; Balicas, L.; Pimenta, M. A.; Terrones, M. New First Order Raman-Active Modes in Few Layered Transition Metal Dichalcogenides. *Sci. Rep.* **2014**, *4*, 4215.
- (37) Kang, D.-H.; Shim, J.; Jang, S. K.; Jeon, J.; Jeon, M. H.; Yeom, G. Y.; Jung, W.-S.; Jang, Y. H.; Lee, S.; Park, J.-H. Controllable Nondegenerate P-Type Doping of Tungsten Diselenide by Octadecyltrichlorosilane. *ACS Nano* **2015**, *9*, 1099–1107.
- (38) Agapov, R. L.; Sokolov, A. P.; Foster, M. D. Protecting TERS Probes from Degradation: Extending Mechanical and Chemical Stability. *J. Raman Spectrosc.* **2013**, *44*, 710–716.
- (39) Opilik, L.; Dogan, Ü.; Szczerbiński, J.; Zenobi, R. Degradation of Silver Near-Field Optical Probes and Its Electrochemical Reversal. *Appl. Phys. Lett.* **2015**, *107*, No. 091109.
- (40) Michaelson, H. B. The Work Function of the Elements and its Periodicity. *J. Appl. Phys.* **1977**, *48*, 4729–4733.
- (41) Fain, S. C., Jr.; McDavid, J. M. Work-Function Variation with Alloy Composition: Ag-Au. *Phys. Rev. B* **1974**, *9*, 5099–5107.
- (42) Pandey, T.; Nayak, A. P.; Liu, J.; Moran, S. T.; Kim, J. S.; Li, L. J.; Lin, J. F.; Akinwande, D.; Singh, A. K. Pressure-Induced Charge Transfer Doping of Monolayer Graphene/MoS₂ Heterostructure. *Small* **2016**, *12*, 4063–4069.
- (43) Raider, S. I.; Berman, A. On The Nature of Fixed Oxide Charge. *J. Electrochem. Soc.* **1978**, *125*, 629–633.
- (44) Deal, B. E. Standardized Terminology For Oxide Charges Associated with Thermally Oxidized Silicon. *IEEE Trans. Electron Devices* **1980**, *27*, 606–608.
- (45) Yeh, P.-C.; Jin, W.; Zaki, N.; Zhang, D.; Liou, J. T.; Sadowski, J. T.; Al-Mahboob, A.; Dadap, J. I.; Herman, I. P.; Sutter, P.; Osgood, R. M. Layer-Dependent Electronic Structure of an Atomically Heavy Two-Dimensional Dichalcogenide. *Phys. Rev. B* **2015**, *91*, 041407.
- (46) Sahin, H.; Tongay, S.; Horzum, S.; Fan, W.; Zhou, J.; Li, J.; Wu, J.; Peeters, F. M. Anomalous Raman Spectra and Thickness-Dependent Electronic Properties of WSe₂. *Phys. Rev. B* **2013**, *87*, 165409.
- (47) Liu, H. J.; Jiao, L.; Xie, L.; Yang, F.; Chen, J. L.; Ho, W. K.; Gao, C. L.; Jia, J. F.; Cui, X. D.; Xie, M. H. Molecular-Beam Epitaxy of Monolayer and Bilayer WSe₂: A Scanning Tunneling Microscopy/Spectroscopy Study and Deduction of Exciton Binding Energy. *2D Mater.* **2015**, *2*, 034004.
- (48) Smyth, C. M.; Addou, R.; McDonnell, S.; Hinkle, C. L.; Wallace, R. M. WSe₂-Contact Metal Interface Chemistry and Band Alignment under High Vacuum and Ultra High Vacuum Deposition Conditions. *2D Mater.* **2017**, *4*, 025084.
- (49) Addou, R.; Smyth, C. M.; Noh, J.-Y.; Lin, Y.-C.; Pan, Y.; Eichfeld, S. M.; Fölsch, S.; Robinson, J. A.; Cho, K.; Feenstra, R. M.; Wallace, R. M. One Dimensional Metallic Edges in Atomically Thin WSe₂ Induced by Air Exposure. *2D Mater.* **2018**, *5*, 025017.
- (50) Chen, C.-H.; Wu, C.-L.; Pu, J.; Chiu, M.-H.; Kumar, P.; Takenobu, T.; Li, L.-J. Hole Mobility Enhancement and P-Doping in Monolayer WSe₂ by Gold Decoration. *2D Mater.* **2014**, *1*, No. 034001.
- (51) Campbell, P. M.; Tarasov, A.; Joiner, C. A.; Tsai, M.-Y.; Pavlidis, G.; Graham, S.; Ready, W. J.; Vogel, E. M. Field-Effect Transistors Based on Wafer-Scale, Highly Uniform Few-Layer P-Type WSe₂. *Nanoscale* **2016**, *8*, 2268–2276.
- (52) Liu, Y.; Stradins, P.; Wei, S.-H. Van der Waals Metal-Semiconductor Junction: Weak Fermi Level Pinning Enables Effective Tuning of Schottky Barrier. *Sci. Adv.* **2016**, *2*, No. e1600069.

Supporting Information

Dry Transfer of van der Waals Crystals to Noble-Metal Surfaces to Enable Characterization of Buried Interfaces

Andrey Krayev¹, Connor S. Bailey², Kiyoun Jo³, Shuo Wang⁴, Akshay Singh⁵, Thomas Darlington⁶, Gang-Yu Liu⁴, Silvija Gradecak⁵, P.James Schuck⁶, Eric Pop², Deep Jariwala^{3*}

1. Horiba Scientific, Novato, CA 94949, USA
2. Department of Electrical Engineering, Stanford University, Stanford, CA, 94305, USA
3. Department of Electrical and Systems Engineering, University of Pennsylvania, Philadelphia, PA 19104, USA
4. Department of Chemistry, University of California, Davis, CA 95616, USA
5. Department of Materials Science and Engineering, Massachusetts Institute of Technology, , Cambridge, MA, 02139 USA
6. Department of Mechanical Engineering, Columbia University, New York, NY, 10027, USA

*Corresponding Author. Email: dmj@seas.upenn.edu

1. Materials Synthesis, Deposition, and Sample Preparation:

Chemical Vapor Deposition of WSe₂

The synthetic monolayer WSe₂ grains were grown in a method similar to that shown for MoSe₂ monolayers previously.¹ Growth substrates, in this case thermally grown SiO₂ on Si, were treated with HMDS and decorated with perylene-3,4,9,10 tetracarboxylic acid tetrapotassium salt (PTAS) to act as a seeding promoter. The main motivation behind the HMDS treatment of our growth substrates specifically stems from our use of perylene-3,4,9,10 tetracarboxylic acid tetrapotassium salt (PTAS) as a seeding promoter. PTAS is a fairly common treatment for CVD growth of TMDs, usually applied as an aqueous solution. We have found that applying the PTAS as small droplets around the edge of our chip results in better TMD growth with a cleaner interface to the substrate.² These droplets are baked and evaporated to remove excess liquid prior to growth, which results in any impurities in the solution depositing as “coffee rings”. In order to maximize our usable area and minimize the size of these “coffee rings”, we utilize an HMDS treatment to make the surface of our substrate hydrophobic, which makes the applied aqueous PTAS droplets smaller. In summary, the use of HMDS does not directly motivate or improve our TMD growth, but practically allows for more growth on a chip without impacting material or electrical quality.

A two-zone quartz tube furnace was loaded with approximately 100 mg of selenium pellets in the first zone and 25 mg of WO₃ in the second, downstream, zone. The treated substrate was placed directly downstream from the WO₃ powder. Under 60 sccm argon flow at atmospheric pressure, the selenium zone was heated to 500°C and the WO₃ zone to 900°C, at which point a 9 sccm flow of H₂ was introduced to aid in reduction of the reaction. After 25 minutes, the H₂ flow was removed and the furnace temperature was ramped down to ambient. These conditions result in direct monolayer growth of WSe₂ with grain sizes on the order of dozens of microns.

Chemical Vapor Deposition of MoS₂

The monolayer MoS₂ growth is carried out at atmospheric pressure in an inert environment (argon). Before the growth is carried out, the 1" CVD tube is heated to ~ 200°C, with continuous evacuation and argon flow for ~ 30 min, to clean the tube of water and other impurities. Subsequently, the tube is brought up to atmospheric pressure with argon. The precursors (sulfur ~ 1 gm and molybdenum oxide powder ~ 20 mg) are kept in alumina boats (in the first and second zones respectively). The substrate (silicon dioxide/ silicon) is kept on top of the boat containing MoO₃ powder (facing down). The flow rate of argon carrier gas is kept at 50 sccm, optimized for single layer growth. The furnace is heated at a rate of 25°C/min with temperature of first (T1) and second (T2) zones targeted at 400°C and 800°C, respectively. After both zones reach the set temperatures, the sulfur boat is pushed to the edge of zone 1 using a pair of magnets, and growth is carried out for 10 min. Subsequently, the tube is gradually brought down to room temperature at a typical rate of 10°C/min.

Gold/Silver Deposition

Thermal gold or silver deposition

100 nm Au or 55 nm Ag thin film was deposited in a high-vacuum evaporator (model DV502-A, Denton Vacuum Inc., Moorestown, NJ). For the Ag thin film, 50 nm Au was successively deposited to prevent Ag oxidation. The Au or Ag was thermally vaporized and deposited onto as-synthesized samples at room temperature and under a base pressure of 5.1×10^{-6} Torr. The evaporation rate was monitored by a quartz crystal monitor (Inficon Inc., East Syracuse, NY) and controlled between 0.10 and 0.15 nm/s. After the deposition, the sample was immediately removed from the chamber and ready for the next step treatment.

Gold sputtering

Gold is sputtered using a EMS Q150T ES coater at low pressures (5×10^{-5} mbar). The rate of deposition is 15 nm/min Au with a sputter current of 20 mA, and a total film thickness of 20 nm.

Electron beam deposition of Au

100 nm Au was deposited using e-beam evaporator (model Lesker PVD75 E-beam Evaporator). The deposition rate was 0.1 nm/s, controlled by QCM under a base pressure of 5×10^{-7} Torr.

Mechanical Exfoliation and Template Stripping:

Mono- and few-layered WSe₂ flakes were deposited on SiO₂ (300 nm) on Si substrates by mechanical exfoliation technique in the glove box (H₂O, O₂ < 0.5 ppm) using a Scotch Tape. The substrate was prebaked in the glove box to avoid possible water traps. After careful flake selection, 100 nm Au was deposited using e-beam evaporation. Using two-component epoxy, the Au layers were fixed to transfer substrate and flipped.

2. Extended Data on CVD grown WSe₂:

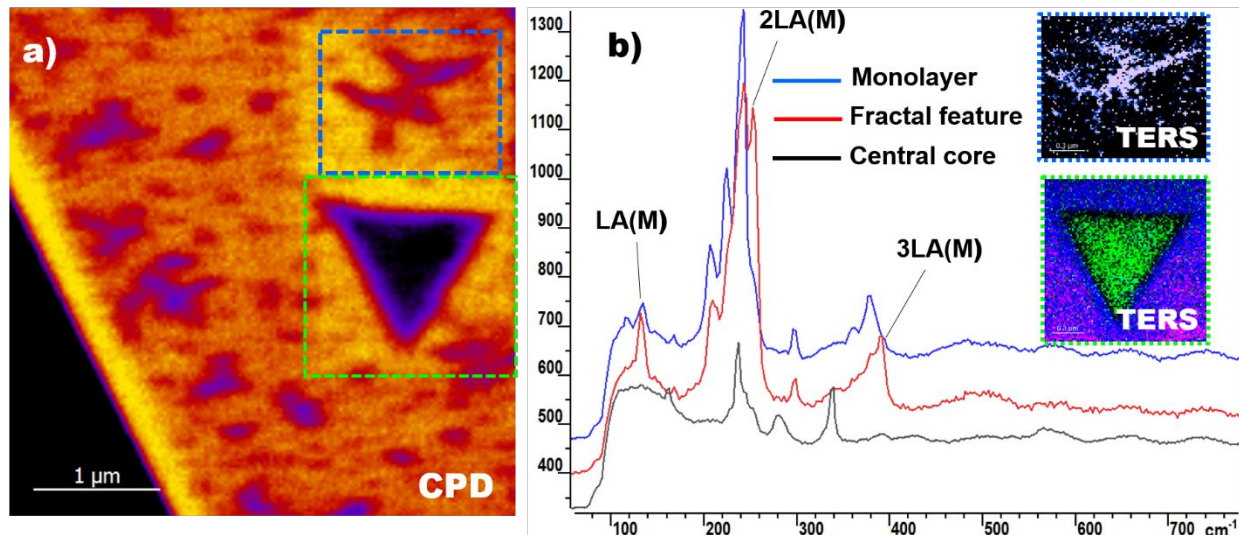


Figure S1. a) CPD image of a gold-transferred WSe₂ crystal from Fig. 2 in main text. TERS maps were collected in the blue and green dotted boxes, featuring lower CPD fractal feature and central triangular core in blue and green boxes respectively. b) averaged TERS spectra from the core (black), monolayer area (blue) and fractal feature (red); spectra are offset vertically for clarity. Upper inset — TERS map (peak position of complex peak in 200 cm⁻¹ to 265 cm⁻¹ range of red spectrum) of the fractal feature; lower insert- TERS map (peak intensity of 336 cm⁻¹ peak (green), complex peak in 200 cm⁻¹ to 265 cm⁻¹ range (blue) and complex peak centered at 380 cm⁻¹ (red)). Both the fractal structure and the central core, both of which show decreased CPD, also have quite different Raman response from the adjacent monolayer.

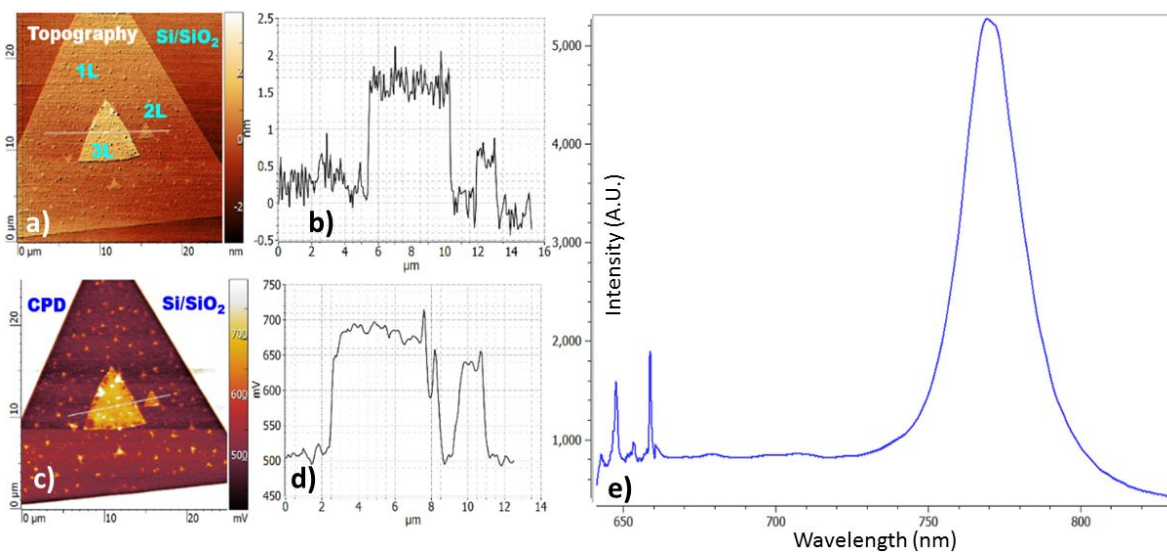


Figure S2. a) topography image and b) corresponding section analysis of as-grown WSe₂ crystal with a central trilayer and a number of bilayer islands; c) CPD image and d) corresponding section analysis; e) – Raman and photoluminescence (PL) spectrum from a location on monolayer part of the crystal showing high PL intensity for monolayer.

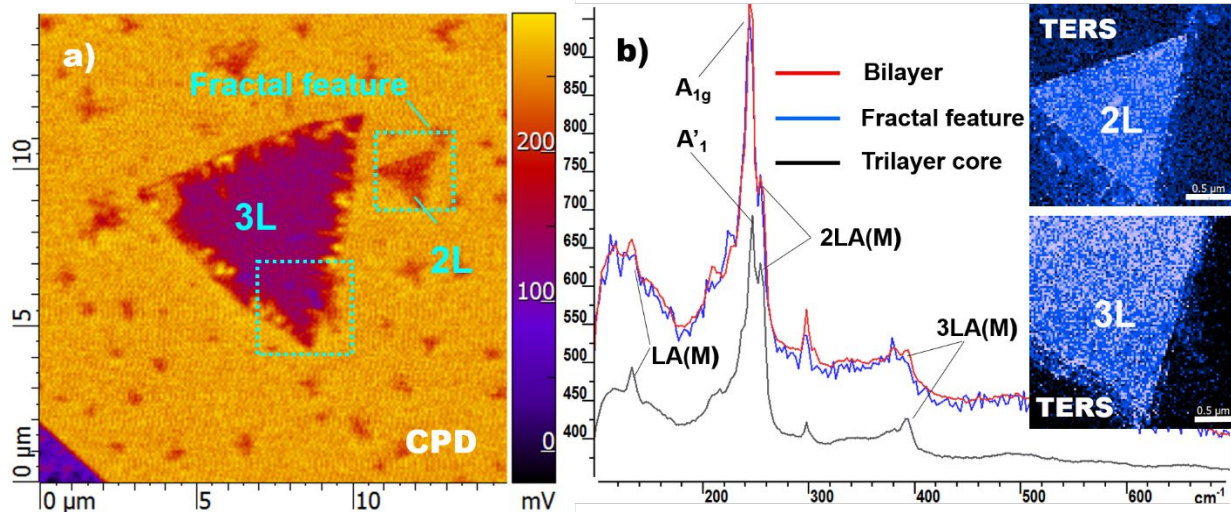


Figure S3. a) Digital zoomed-in CPD image of the crystal in Fig. 3 of main text after gold transfer. TERS maps were collected over the areas marked with blue dotted boxes marked with blue dotted boxes b) averaged TERS spectra from bilayer (red), fractal bilayer feature (blue) and trilayer core (black). As can be clearly seen from these spectra, relative intensity of the 2LA(M) peak compared to A_{1g} peak is practically identical for the triangular and fractal bilayer features, while it increases for the trilayer core. In the insert- TERS maps (peak position of the complex peak within 230-270 cm^{-1} range).

3. Characterization and analysis of CVD grown MoS_2 samples:

In the first series gold layer was deposited on MoS_2 crystals via sputtering, the rest of the transfer procedure was the same as in case of WSe_2 . MoS_2 crystals were successfully transferred from the growth substrate, featuring very shallow roughness of the surface and familiar concentric triangular features with lower value of the surface potential in the CPD images of some MoS_2 crystals (Fig. S4). Despite the similarity of the sample surface morphology and CPD distribution to the case of gold-assisted transfer of WSe_2 , TERS map of the of MoS_2 crystal showed almost negligible Raman response from the monolayer areas and only fairly weak A_{1g} and E_{2g} peaks intensity over the central triangular feature. This was specifically surprising taking into account high background signal in TERS spectra, which was an indication of strong enhancement of the TERS probe.

To clarify the reasons of such poor TERS performance of gold –assisted transferred MoS_2 crystals, we repeated the experiment, this time depositing gold via thermal evaporation following the same protocol and using exactly the same deposition system that was used for experiments with WSe_2 crystals. Transfer of these samples was also successful, and though there were some pits on the exposed gold surface, they did not affect our ability to perform SKM and TERS characterization.

SKM characterization of the sample showed some significant differences in the CPD signal across the transferred flake, though the contrast was not as sharp as in case of WSe_2 . The TERS map collected over the internal part of the flake that featured significant variation of the CPD value (Fig. S5), featured high quality TERS spectra with strong signal-to noise ratio and showing presence of multiple resonant peaks in addition to A_{1g} and E_{2g} modes. Major variations in TERS

spectra were related to the intensity of the background and the intensity of complex resonant modes LA(\sim K)+TA(\sim K), following the peak assignment of Carvalho *et al.*² at around 423 cm⁻¹. What was specifically interesting was that the TERS map of the peak position for 380-440 cm⁻¹ spectral range showed reasonably good correlation with the CPD image. On the other hand, the map representing both the Raman peak and the background intensity (peak area) clearly showed a triangular shaped feature in the upper portion of the flake. This feature did not have a corresponding counterpart in the CPD image. Further, a number of small 100-200 nm “bubble-like” features showing increased intensity of both the Raman peaks and the background were observed as seen in Fig. S6. This observation again highlights the power of TERS imaging that can reveal features unobservable otherwise.

Overall, we must conclude that while the gold-assisted transfer of MoS₂ was possible in principle, SKM and TERS data obtained on transferred crystals were not as clear and unambiguous as for WSe₂. This could likely be due to presence of some growth-specific “contamination” layer between the MoS₂ crystals and the SiO₂/Si substrate which prevents direct access to the tip and will have to be clarified in a follow-up study.

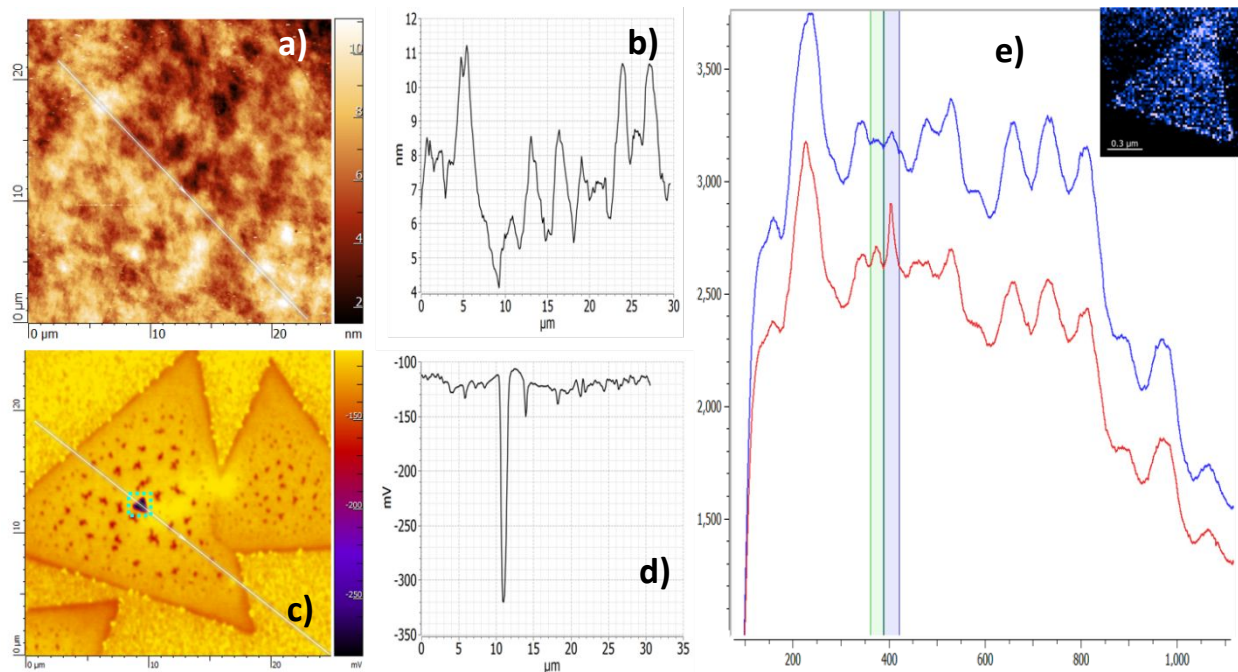


Figure S4. a) Topography of the MoS₂ sample transferred with sputtered gold; b) corresponding section analysis; c)- CPD image of the same area showing a signature of thicker triangular core in the center of bigger crystal; d)- corresponding section analysis showing significant (over 150 mV) drop of the surface potential over the central core; e)- TERS map (intensity of 408 cm⁻¹ peak) collected over the dotted square in c) and typical spectra from the monolayer (blue) and central core (red).

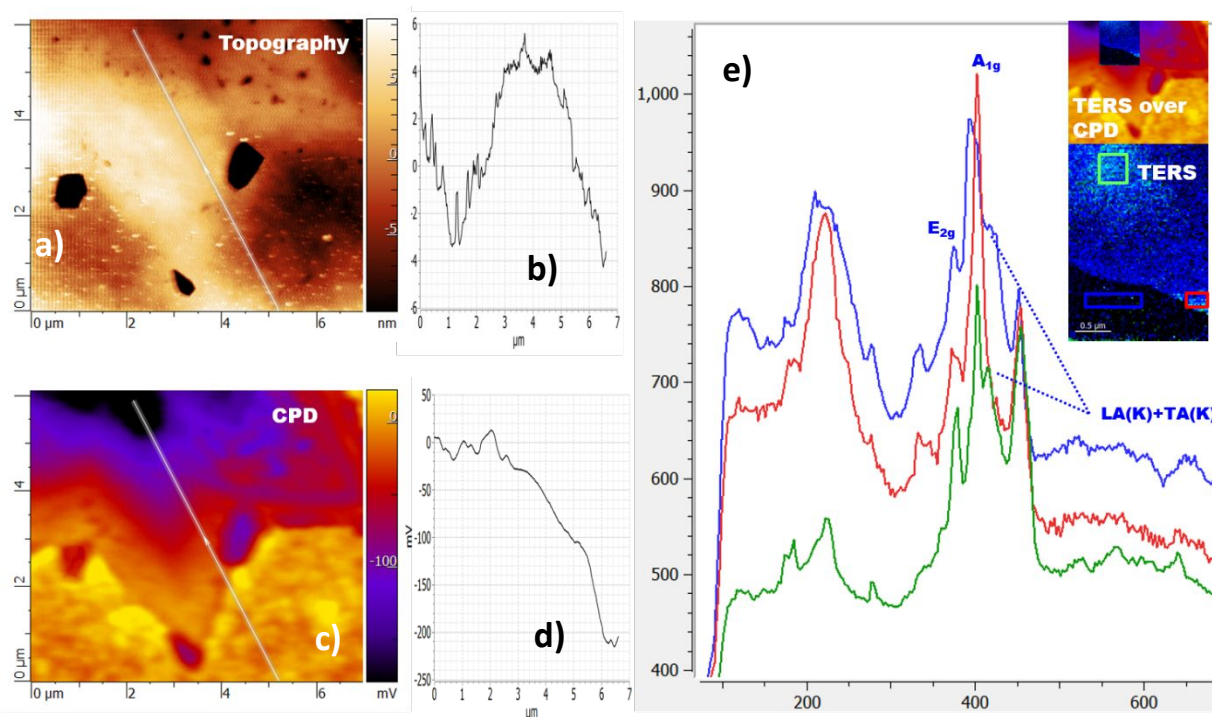


Figure S5. a) topography of MoS₂ sample transferred with thermally evaporated gold; b)-corresponding section analysis; c)- CPD image of the same area; d) –section analysis of the CPD image; e) averaged TERS spectra and corresponding TERS maps (380-440 cm⁻¹ peak position) with color coded boxes (inset) showing very sharp borderlines, which additionally confirms near-field nature of the recorded signal. (Units: x axis: Wavenumber (cm⁻¹), y axis: Intensity (A.U.))

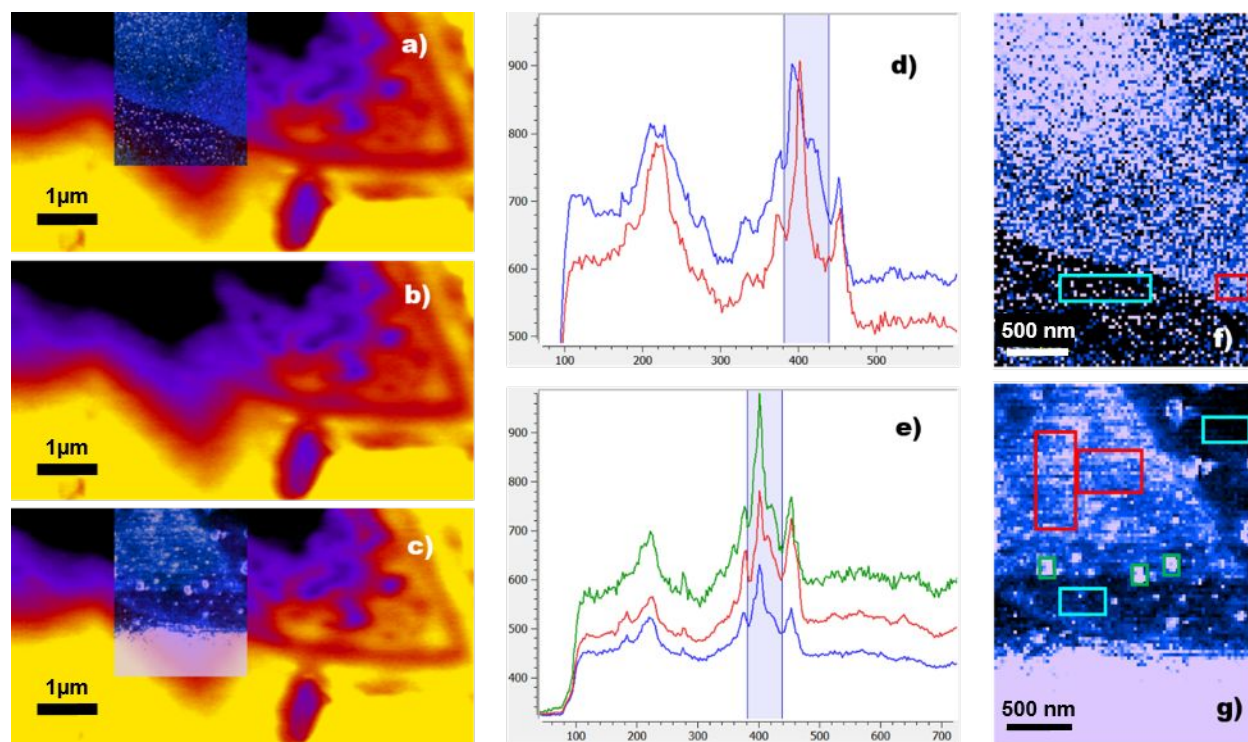


Figure S6. MoS₂ sample transferred with thermally evaporated gold. Same area as in Fig.S5. a)-TERS map (380-440 cm⁻¹ peak position) overlaid over CPD; b) corresponding CPD image; c) TERS map (380-440 cm⁻¹ peak area including background) overlaid over CPD. A sharp triangular feature is clearly seen in this map that does not have a counterpart in the CPD image; d) averaged TERS spectra from correspondingly colored areas in f); e) averaged TERS spectra from correspondingly colored areas in g); f)- TERS map (380-440 cm⁻¹ peak position); g) TERS map of the same area representing 380-440 cm⁻¹ peak area including background.

5. CPD and TERS mapping of Au-transferred direct exfoliated WSe₂

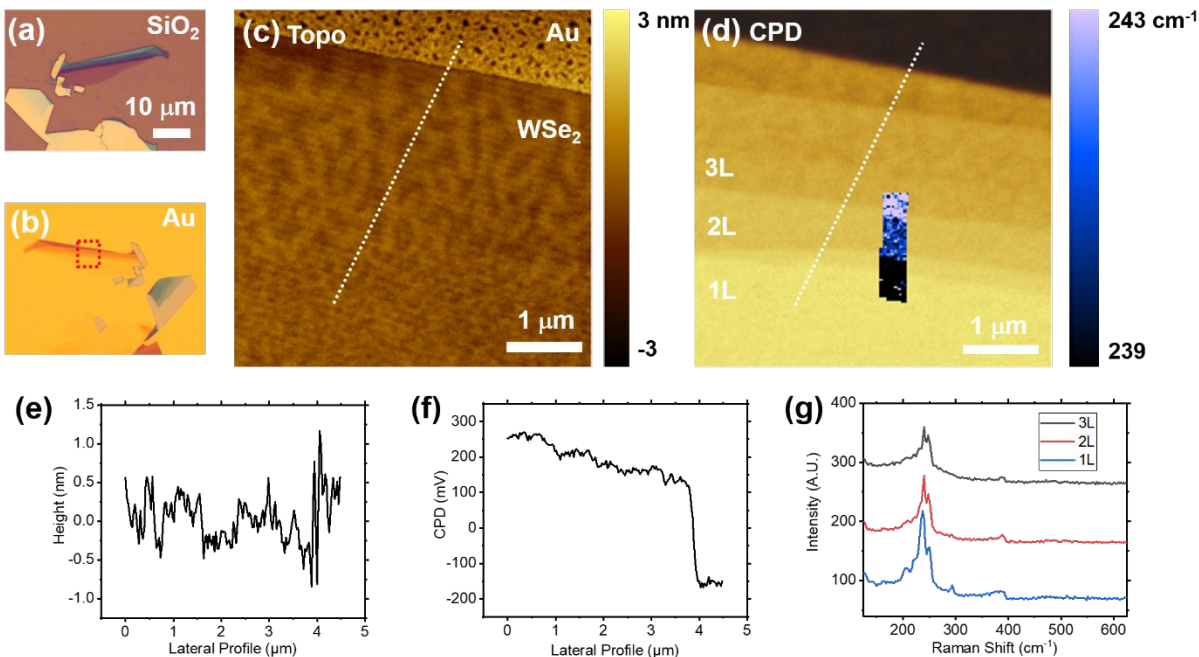


Figure S7. Optical Image of (a) direct exfoliated WSe₂ on SiO₂/Si and (b) Au-transferred WSe₂ original flake. (c) Topography and (d) CPD of highlighted red box region in (b) and corresponding lateral profile of (e) topography, (f) CPD. Blue box in (d) is TERS peak position mapping. (g) TERS spectrum corresponding to (d).

6. Far-Field Raman Spectra

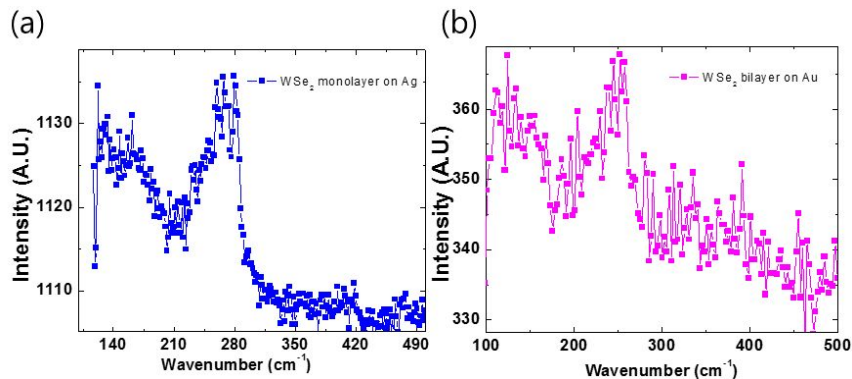


Figure S8. (a) Far-field Raman spectrum of CVD grown monolayer WSe₂ flake on Ag. No clear Raman signal is evident in comparison to near-field signals in Figure 3 and 4 of main manuscript (b) Far-field Raman

spectrum of CVD grown monolayer WSe₂ flake on Ag. No clear Raman signal is evident in comparison to near-field signals in Figure 3 and 4 of main manuscript thereby rendering comparison difficult.

References:

1. Smithe, K. K. H.; Krayev, A. V.; Bailey, C. S.; Lee, H. R.; Yalon, E.; Aslan, Ö. B.; Muñoz Rojo, M.; Krylyuk, S.; Taheri, P.; Davydov, A. V.; Heinz, T. F.; Pop, E. Nanoscale Heterogeneities in Monolayer MoSe₂ Revealed by Correlated Scanning Probe Microscopy and Tip-Enhanced Raman Spectroscopy *ACS Applied Nano Materials*, **2018**, *1*, 572-579.
2. Kirby K H Smithe, Chris D English, Saurabh V Suryavanshi and Eric Pop, Intrinsic Electrical Transport and Performance Projections of Synthetic Monolayer MoS₂ Devices. *2D Materials*, **2017**, *4* 011009
3. Carvalho, B. R.; Wang, Y.; Mignuzzi, S.; Roy, D.; Terrones, M.; Fantini, C.; Crespi, V. H.; Malard, L. M.; Pimenta, M. A. Intervalley Scattering by Acoustic Phonons in Two-Dimensional MoS₂ Revealed by Double-Resonance Raman Spectroscopy. *Nature Communications* **2017**, *8*, 14670.